TURBULENCE WITH SPATIALLY FIXED ANISOTROPIC VISCOSITY

Hanna Berning, Daniel Stalder, Tommaso Ciuti and Thomas Rösgen
Institute of Fluid Dynamics
ETH Zurich
Sonneggstr. 3, 8092 Zurich, Switzerland
berningh@ethz.ch, dstalder@student.ethz.ch, tommaso.ciuti@hotmail.it, roesgen@ethz.ch

Davide Gatti
Institute of Fluid Mechanics
Karlsruhe Institute of Technology
Kaiserstraße 10, 76131 Karlsruhe, Germany
davide.gatti@kit.edu

ABSTRACT

Experimentally and numerically, we investigate the impact of a spatially homogeneous, direction-dependent tensorial viscosity on a turbulent flow. The anisotropy is induced by the magnetic alignment of prolate tracer particles in an external magnetic field. In the experiment, a spatial fixation of global flow modes in a von Kármán flow is observed. In the direct numerical simulation, the anisotropy dominates at small scales and causes field-parallel alignment of vortices and a decrease of the energy spectra in the same direction.

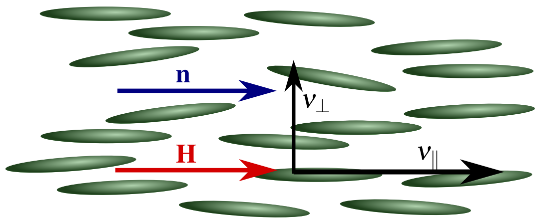

Figure 1: Schematic of anisotropic viscosity induced by the alignment of elongated particles with an external magnetic field **H**. The average alignment direction can be described with a director **n**.

INTRODUCTION

Well established relations such as Kolmogorov's first similarity hypothesis are based on a scalar viscosity ν and the assumption of small-scale isotropy, so that turbulence statistics at small scales are uniquely determined by this viscosity and the dissipation rate ε. Following the work by Grünberg (2016), we ask how turbulent statistics are modified if the viscosity is of tensorial nature. In particular, we pose the question of whether and how small-scale anisotropy affects the larger-scale features of the flow. As opposed to frequently studied flows with various anisotropic particles (Butler & Snook, 2018; Winkler *et al.*, 2004; Voth & Soldati, 2017), geometrical constraints (Antonia *et al.*, 1994) or anisotropic forcing (Julien *et al.*, 2018) where anisotropy at the small scales is induced by the flow itself, here the viscous anisotropy is imposed *a priori* with a fixed orientation in space. This can be achieved with magnetic, anisotropic particles much smaller than the Kolmogorov length η which are aligned with their long axis in the direction of a magnetic field. The resulting viscosity will be lower in the direction parallel than in the direction perpendicular to the particle long axis (Fig. 1, $\nu_\perp > \nu_\parallel$).

We tackle the problem both numerically and experimentally.

EXPERIMENT IN A VON KÁRMÁN FLOW

Setup

As an experimental configuration, we choose a von Kármán flow due to its strong turbulence in a small flow volume (Fig. 2).

The anisotropic viscosity is introduced by a magnetic induction field **B** of up to 80 mT which acts on magnetic micro particles dispersed in water. These consist of a magnetite core and a silica coating to prevent agglomeration and chain formation (Fig. 3). With an average length of 1.9 µm = 0.03 η and an aspect ratio of 5.7, the particles have a Stokes number of around 1×10^{-5} and act like passive tracers. The Mason number $Mn \approx 3.5 \times 10^{-3}$ indicates that the magnetic moment dominates over the hydrodynamic influence. A dilute suspension approaching the semi-dilute state (volume fraction $\Phi \approx 0.02$ with dimensionless number density $nL^3 \approx 0.78$) allows to observe maximal anisotropic effects while still limiting the interaction between the particles.

The turbulence properties are investigated using ultrasonic techniques. An ultrasonic profiler (UDV, DOP3010 from Signal Processing SA) as an Eulerian measurement captures global effects throughout the cell (Fig. 2a). It records the velocity component in the emission direction along transverse lines through the cell centre. In addition, a custom-built ultrasound particle tracking system, Fig. 2b, allows to spatially and temporally resolve Lagrangian trajectories in the centre of the

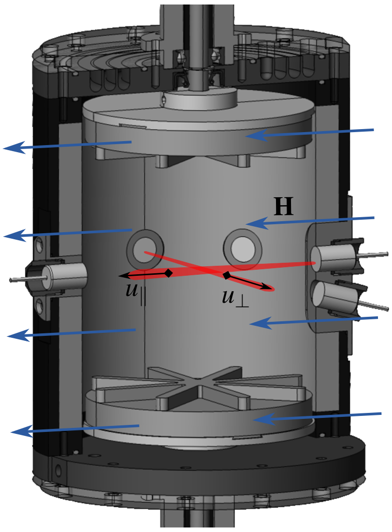

(a) Eulerian ultrasound velocity measurement along a transverse line.

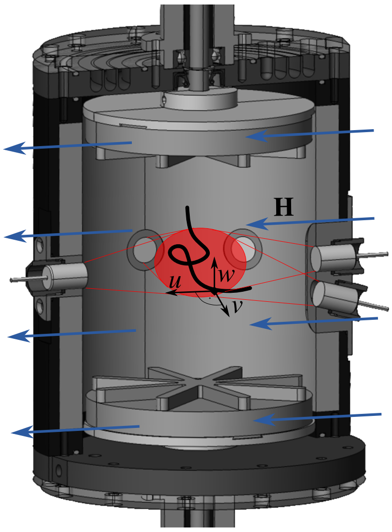

(b) Lagrangian ultrasound particle tracking in centre of cell.

Figure 2: Measurement techniques in a von Kármán flow with superimposed magnetic field **H**.

cell (Grünberg, 2016). We compare the velocity statistics in the direction of the magnetic field and perpendicular to it.

We apply both a constant forcing (C), where the discs are continuously counter-rotating, and a pseudo-random forcing (PRBS), where the sense of disc rotation is reversed irregularly. In the former case, a large scale structure emerges, which is characterized by an in- and outflow in the transverse plane (compare gray curves in Fig. 4 and left sketch in Fig. 6). The random forcing suppresses this mean-flow instability and ensures isotropy in the transverse plane (Berning *et al.*, 2017).

Results

In Fig. 4, the central moments of the transverse velocities of the continuously forced flow show that the roughly isotropic moment profiles diverge for the two directions under the influence of a magnetic field. A pinning of the global modes occurs, where the inflow orients in the field-parallel direction. The limiting case of pure in- or outflow mode, indicated with gray lines, is approached for all moments.

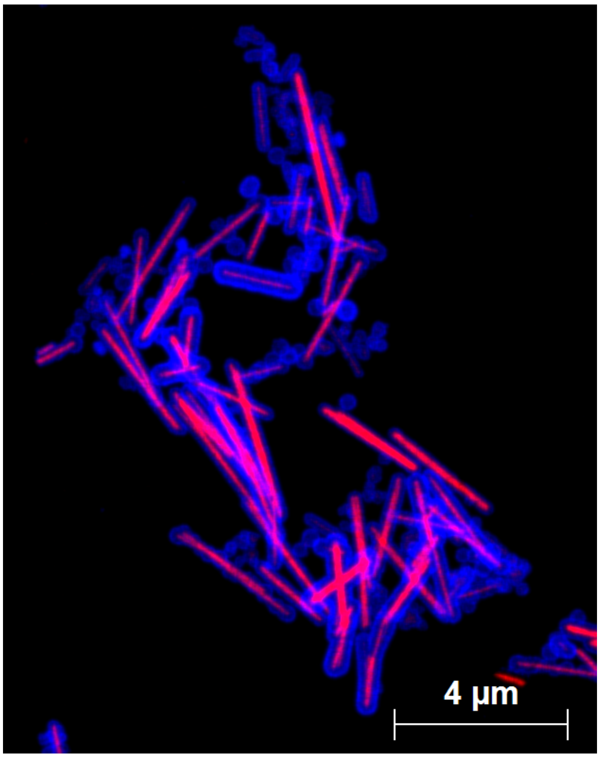

Figure 3: TEM images of the nanorods including an element analysis showing silica (blue) and iron (red) content.

This finding is supported by quasi-simultaneous recordings of the perpendicular transducers. Fig. 5 shows the joint probability of the projection of the instantaneous velocity profiles onto the inflow profile. A positive correlation coefficient P indicates an inflow state while a negative coefficient represents an outflow observation. While in the field-free case the narrow negative correlation proves near-equal probability of the modes for both transducers, with the alignment of the magnetic particles the distribution becomes asymmetric and inflow prevails in the alignment direction. We hypothesize that the flow structure, originally rotating in azimuthal direction, orients as in the sketch in Fig. 6 in the transverse meridional plane.

This large-scale anisotropy leaves a footprint on small-scale quantities in the centre of the cell, such as the Lagrangian Taylor microscale, which is depicted Fig. 7. The small-scale correlations are larger in the field-parallel direction compared to the remaining directions. For the randomly forced flow, however, no significant small-scale anisotropy is detected within the measurement uncertainty. The slight trend observed in the Taylor microscales may as well be a large-scale imprint due to the remaining 10% outflow probability. In agreement with the moment profiles, the ratio of the Lagrangian second-order structure functions, Fig. 8, reveals a small initial anisotropy already without the application of a magnetic field. The ratio increases towards large lags, confirming the scale-dependence of the anisotropy, which is primarily emerging at large scales.

DIRECT NUMERICAL SIMULATION
Setup

Complementary to the experiment, the phenomenon is investigated numerically. The anisotropy can be modeled using Leslie and Ericksen's director theory for liquid crystals which

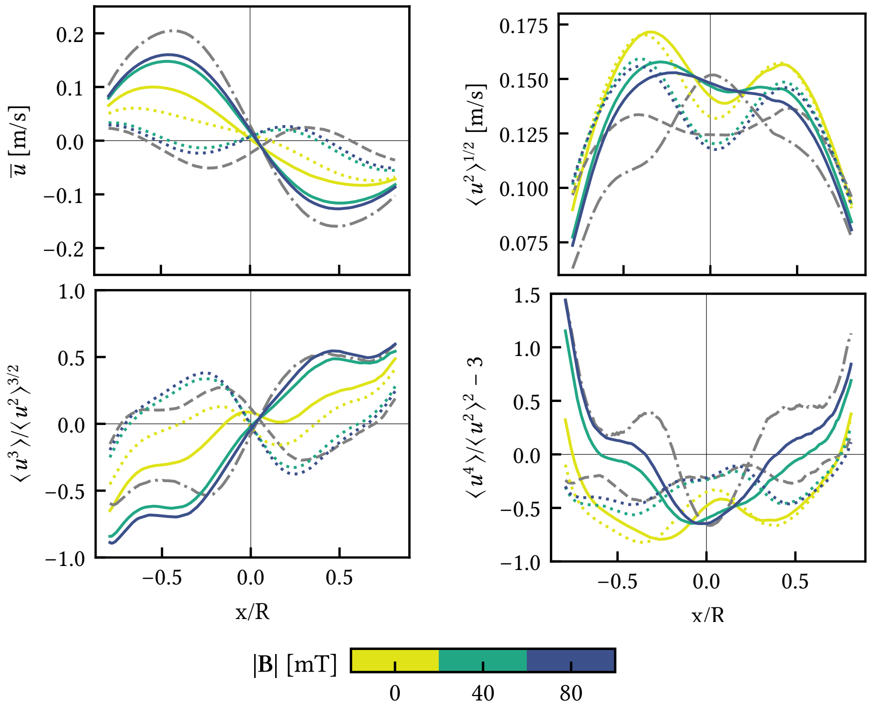

Figure 4: Profiles of velocity moments of transverse velocity components for different magnetic induction field strengths $|\mathbf{B}|$. Coloured solid line: direction parallel to magnetic field, dotted line: direction perpendicular to magnetic field. Gray lines: inflow (dashed) and outflow (dash-dotted) profiles without magnetic field.

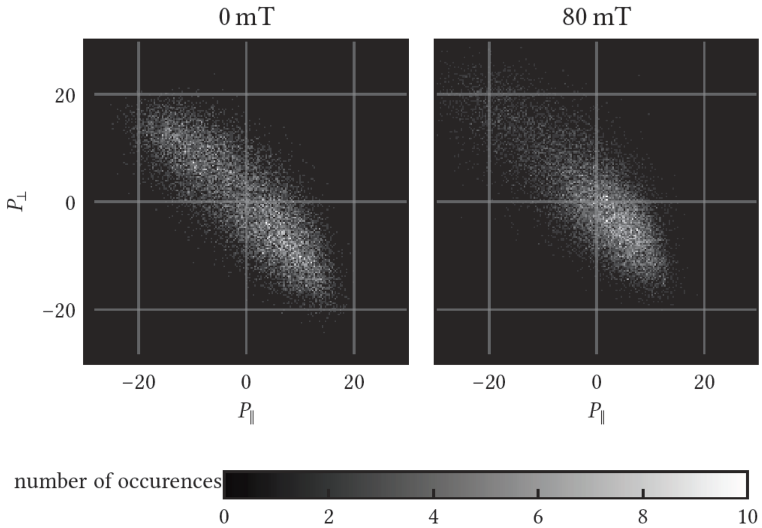

Figure 5: Joint probability density function of instantaneous projections of the transverse velocity components parallel and perpendicular to the magnetic field onto the inflow profile. Results are presented without and with influence of the magnetic field for constant forcing.

reduces the unknown viscosity tensor of 4th order to only six Leslie coefficients α_i (Leslie, 1966). The governing equations for an incompressible fluid are:

$$\rho \frac{\partial \mathbf{u}}{\partial t} + \rho(\mathbf{u} \cdot \nabla)\mathbf{u} = -\nabla p + \nabla \cdot \boldsymbol{\tau} \tag{1}$$

$$\begin{aligned} \boldsymbol{\tau} =& \alpha_1(\mathbf{nn} : \mathbf{D})\mathbf{nn} + \alpha_2 \mathbf{nN} + \alpha_3 \mathbf{Nn} + \alpha_4 \mathbf{D} + \\ & \alpha_5 \mathbf{nn} \cdot \mathbf{D} + \alpha_6 \mathbf{D} \cdot \mathbf{nn} \end{aligned} \tag{2}$$

with

$$\mathbf{D} = \frac{1}{2}\left(\nabla \mathbf{u} + \nabla \mathbf{u}^T\right) \tag{3}$$

$$\mathbf{N} = \dot{\mathbf{n}} - \boldsymbol{\omega} \times \mathbf{n} \tag{4}$$

Ilg & Kröger (2002) derived an expression for the Leslie coefficients accounting for the effect of non-interacting rigid magnetic ellipsoids that are aligned in a magnetic field (Fig. 1). With a strong magnetic field $\mathbf{H}$ the parameters approach the

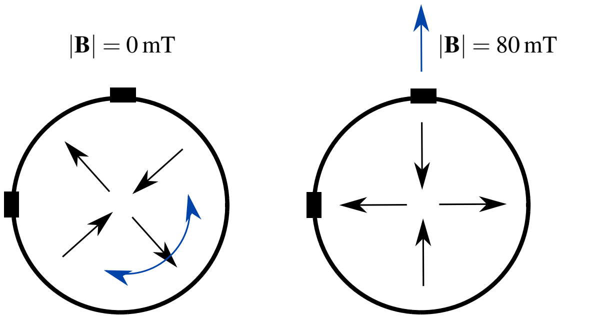

Figure 6: Sketch of the mode pinning under alignment of anisotropic magnetic particles in the transverse plane of a continuously forced von Kármán flow.

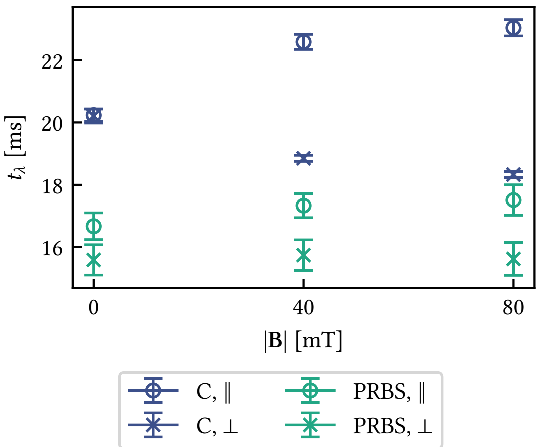

Figure 7: Temporal taylor microscales τ_λ of transverse velocity components aligned in field-parallel or perpendicular direction using constant (C) and random (PRBS) forcing.

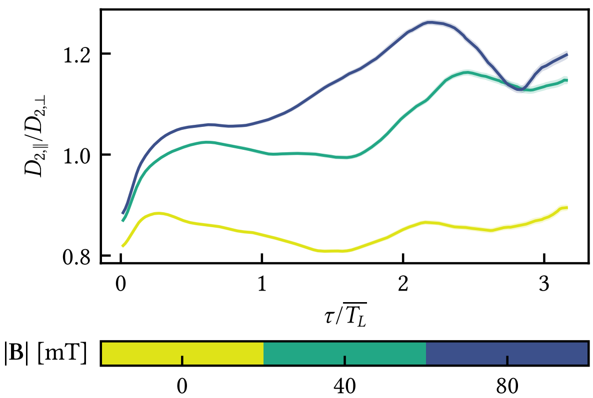

Figure 8: Effect of magnetic field strength on the ratio of the Lagrangian second-order structure functions in transverse directions using constant forcing. $\overline{T}_L$ denotes the Lagrangian integral time averaged over the transverse directions.

limiting case of a fixed director **n**, corresponding to a spatially homogeneous and constant anisotropic viscosity. The Leslie-coefficients can then be computed *a priori*[1].

A direct numerical simulation (DNS) allows to fully resolve all scales of the problem and to characterize the effect of the anisotropy on the various scales of the flow. We perform a DNS with the spectral solver ISODNS (Carini & Quadrio, 2010) to study a periodic box of homogeneous turbulence. Statistical steadiness is imposed via a linear low-wavenumber forcing (Lamorgese *et al.*, 2005).

The stress tensor is implemented in the velocity-vorticity formulation of ISODNS and validated at $Re_{\lambda,eff} = 35$ against simulations with the spectral element solver Nek5000, where the analytically simpler formulation in natural variables and a random low-wavenumber forcing (Eswaran & Pope, 1988; Weiss *et al.*, 2019) are employed.

Next to the experimental volume fraction $\Phi = 0.02$, a large volume fraction, $\Phi = 0.2$ is studied. In a real experiment, the latter would violate the assumption of non-interacting particles, but numerically it allows to study enhanced effects. For comparison with the experiment, the particle aspect ratio is chosen to be 5.7 and 6.5, respectively. The ratios between the largest and the smallest Miesowicz-viscosities, resulting from particle-alignment in streamwise and gradient direction of a two-dimensional flow, are 1.6 and 6.5. The field and director are pointing in the second direction (y-axis).

Results

The results presented here are based on studies at low to moderate effective Reynolds numbers, $Re_{\lambda,\mathrm{eff}} = 35-92$, where an effective Reynolds number can be defined using the mean transverse Taylor microscale ($\lambda_{\mathrm{T,eff}}$) and an effective viscosity ν_{eff}:

$$Re_{\lambda,\mathrm{eff}} = \frac{u_{\mathrm{rms}}\lambda_{\mathrm{T,eff}}}{\nu_{\mathrm{eff}}} \tag{5}$$

The effective viscosity is defined as

$$\nu_{\mathrm{eff}} = \frac{P_F}{2\langle s_{ij}s_{ij}\rangle} \tag{6}$$

with P_F as the constant energy injection rate of the forcing and s_{ij} the rate-of-strain tensor. We focus on the results at $\Phi = 0.2$. The lower particle volume fraction exhibits the same trends, albeit with such small magnitude that effects might be difficult to resolve experimentally. The Reynolds number does not affect the trends in the investigated range.

In Fig. 9, we present the spatial microscales $\lambda^{ii,j}$, extracted from the autocorrelation function of the i-th velocity component in the j-th direction, normalised by the respective mean in transverse and longitudinal direction. The spatial Taylor microscales are much larger in the field-parallel direction. Exemplary, the results from both solvers are shown. The isotropy in the field-free case is better achieved with Nek5000 using the random forcing. The anisotropic simulations with ISODNS, however, yield qualitatively and quantitatively comparable results. The good agreement of both codes – with improved isotropy resulting from the random forcing – is also found in the remaining analyses.

In addition to the autocorrelation functions, also the related one-dimensional energy spectra contain direction- and scale dependent information. They are computed for the i-th

[1] In some of the equations of Ilg & Kröger (2002) typographical errors were found. In agreement with the authors, the corrected equations are:

$$(28) \quad \alpha_4 - 2\eta_{0,r} = -4\eta_0^\Phi\left(\frac{2}{7}Q_{32}S_2 + \frac{1}{35}Q_{23}S_4\right)$$

$$(29) \quad \alpha_5 + \alpha_6 = \frac{8}{7}\eta_0^\Phi(3Q_{32}S_2 + Q_{23}S_4)$$

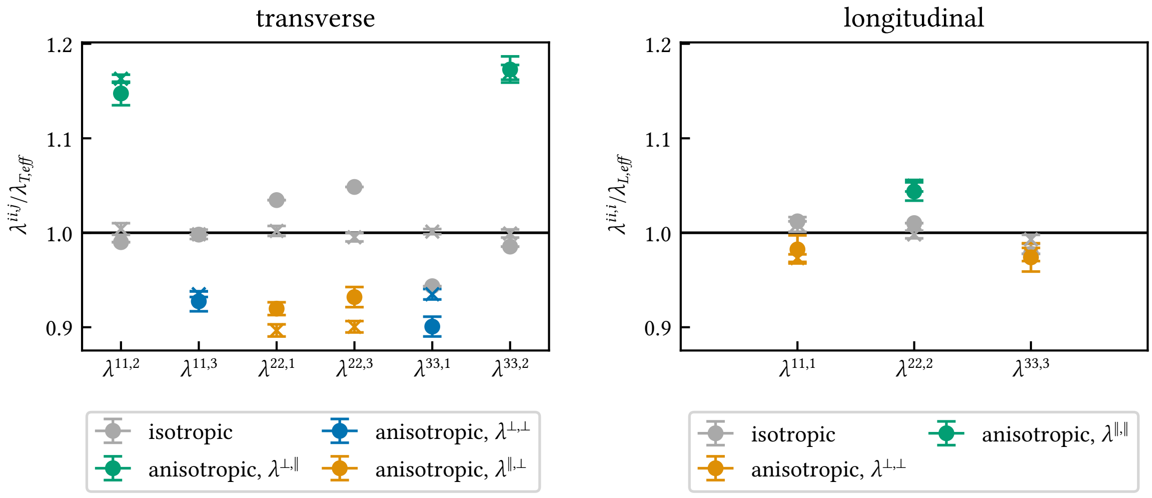

Figure 9: Spatial transverse and longitudinal Taylor microscales $\lambda^{ii,j}$ at $Re_{\lambda,eff} = 35-40$ for directions parallel and perpendicular to the magnetic field. Circles: ISODNS, crosses: Nek5000. The values are normalized by their respective means.

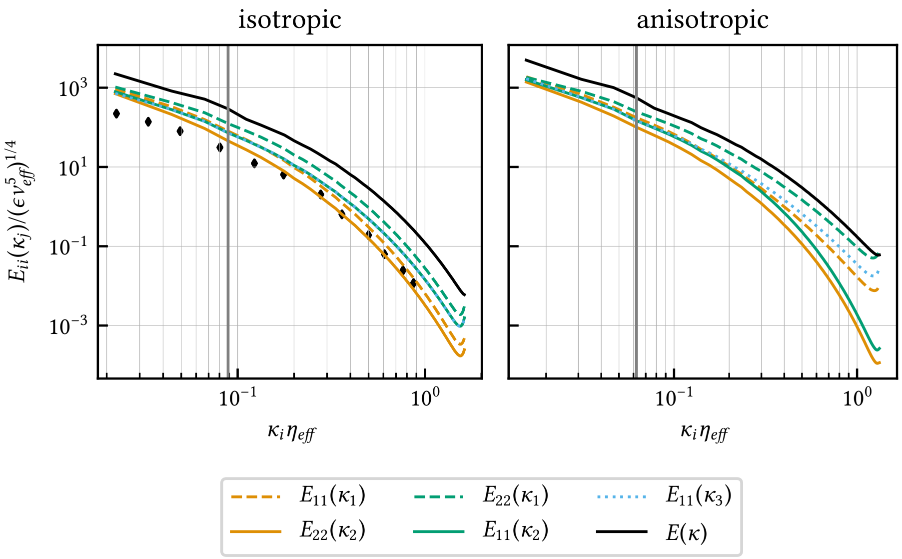

Figure 10: Selected one-dimensional energy spectra from ISODNS with $\Phi = 0.2$ at $Re_{\lambda,eff} = 72-96$. Yellow: longitudinal spectra, green and blue: transverse spectra. Solid lines: in second wavenumber direction. Left: isotropic, right: anisotropic simulation. The gray line indicates the boundary of the forcing shell. Additionally, $E_{11}(\kappa_1)$ from grid turbulence measurements at $Re_\lambda = 72$ is shown (CBC 1971 after Pope (2000)).

velocity component in the j-th wavenumber direction from the velocity spectrum tensor Φ_{ij}, which is the Fourier transform of the two-point correlation (Pope, 2000).

$$E_{ii}(\kappa_j) = 2\iint_0^\infty \Phi_{(i)(i)}(\boldsymbol{\kappa})d\kappa_m d\kappa_n \qquad (7)$$

Here, j,m,n are non-equal directional indices and no summation over indices $(i)(i)$ is employed. The energy spectra exhibit a strong wavenumber-dependent anisotropy (Fig. 10). Regardless of the velocity component, the kinetic energy decreases in the direction of the director and the longitudinal and transverse component approach each other in this direction.

For both energy spectra and Taylor microscales, the influence of the direction exceeds the impact of the velocity component. Variations in the field-parallel direction are much larger than in the perpendicular directions, irrespective of the velocity component analysed. Furthermore, the effects are more pronounced for the transverse quantities compared to the longitudinal ones.

Finally, the structure of the flow is of interest. The eigenvalues of the velocity gradient tensor are used to compute the vortex orientation $\mathbf{v}_r$ and the swirling strength λ_{ci} employing an enhanced criterion (Zhou *et al.*, 1999; Chakraborty *et al.*, 2005). The probability density functions of the vortex orientation show a strong dependence on the swirling strength (Fig. 11). At higher swirling strengths, which correspond to smaller eddies, the vortices are increasingly aligned in the direction of the director. Interestingly, an opposite effect appears for low swirling strengths.

CONCLUSIONS

The effects of a spatially fixed anisotropic viscosity on turbulence properties are investigated in fully resolved numerical simulations and experiments. The anisotropy is induced

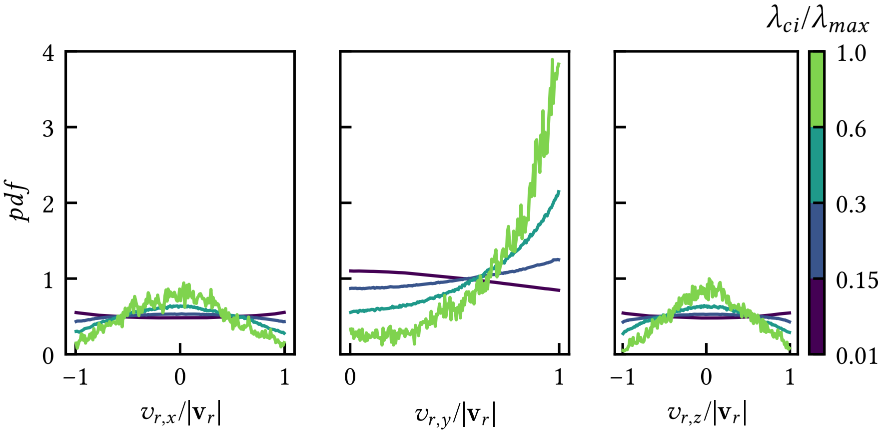

Figure 11: PDFs of vortex orientation for different swirling strength ranges computed with the enhanced criterion for $\Phi = 0.2$ and ISODNS at $Re_{\lambda,\mathrm{eff}} = 72 - 96$.

via the alignment of prolate magnetic particles in a magnetic field. In the experiment, we observe a directional fixation of a global flow structure. This mode pinning leaves an imprint on all scales. For a randomly forced flow without dominant flow structure, no small-scale anisotropy can be detected within the measurement uncertainty. On the other hand, the simulations exhibit a strong anisotropy emerging directly from the highest wavenumbers, propagating and decreasing towards lower wavenumbers. In contrast to the commonly implied energy cascade where isotropy is regained at small scales even if the energy input is anisotropic, here, the opposite effect is therefore present. In the direction of the smaller viscosity, energy decreases and vortices align at small scales. This is reflected in an increase of the Taylor microscales in this direction.

Acknowledgments

The authors gratefully acknowledge Dr. Robin Schäublin of ScopeM for support and assistance with the Transmission Electron Microscopy (TEM) work.

References

Antonia, R. A., Djenidi, L. & Spalart, P. R. 1994 Anisotropy of the dissipation tensor in a turbulent boundary layer. *Physics of Fluids* **6** (7), 2475–2479.

Berning, H., Grünberg, T. & Rösgen, T. 2017 Suppression of Large Scale Structures in a Turbulent von Kármán Flow using Random Forcing. *10th International Symposium on Turbulence and Shear Flow Phenomena* .

Butler, J. E. & Snook, B. 2018 Microstructural Dynamics and Rheology of Suspensions of Rigid Fibers. *Annual Review of Fluid Mechanics* **50** (1), 299–318.

Carini, M. & Quadrio, M. 2010 Direct-numerical-simulation-based measurement of the mean impulse response of homogeneous isotropic turbulence. *Physical Review E* **82** (6), 066301.

Chakraborty, P., Balachandar, S. & Adrian, R. J. 2005 On the relationships between local vortex identification schemes. *Journal of Fluid Mechanics* **535**, 189–214.

Eswaran, V. & Pope, S.B. 1988 An examination of forcing in direct numerical simulations of turbulence. *Computers & Fluids* **16** (3), 257–278.

Grünberg, Tim 2016 Response of a turbulent flow to anisotropy at the molecular scale. PhD thesis, ETH Zurich.

Ilg, P. & Kröger, M. 2002 Magnetization dynamics, rheology, and an effective description of ferromagnetic units in dilute suspension. *Physical Review E* **66** (2).

Julien, K., Knobloch, E. & Plumley, M. 2018 Impact of domain anisotropy on the inverse cascade in geostrophic turbulent convection. *Journal of Fluid Mechanics* **837**.

Lamorgese, A. G., Caughey, D. A. & Pope, S. B. 2005 Direct numerical simulation of homogeneous turbulence with hyperviscosity. *Physics of Fluids* **17** (1), 015106.

Leslie, F. M. 1966 Some constitutive equations for anisotropic fluids. *The Quarterly Journal of Mechanics and Applied Mathematics* **19** (3), 357–370.

Pope, S.B. 2000 *Turbulent Flows*. Cambridge University Press.

Voth, G. A. & Soldati, A. 2017 Anisotropic Particles in Turbulence. *Annual Review of Fluid Mechanics* **49** (1), 249–276.

Weiss, P., Oberle, D., Meyer, D. W. & Jenny, P. 2019 Impact of turbulence forcing schemes on particle clustering. *Physics of Fluids* **31** (6), 061703.

Winkler, R. G., Mussawisade, K., Ripoll, M. & Gompper, G. 2004 Rod-like colloids and polymers in shear flow: a multi-particle-collision dynamics study. *Journal of Physics: Condensed Matter* **16** (38), S3941–S3954.

Zhou, J., Adrian, R. J., Balachandar, S. & Kendall, T. M. 1999 Mechanisms for generating coherent packets of hairpin vortices in channel flow. *Journal of Fluid Mechanics* **387**, 353–396.